



# Three-dimensional imaging system with both improved lateral resolution and depth of field considering non-uniform system parameters

HUI YUN,<sup>1</sup> ANABEL LLAVADOR,<sup>2</sup> GENARO SAAVEDRA,<sup>2</sup> AND MYUNGJIN CHO<sup>1,\*</sup> 

<sup>1</sup>Department of Electrical, Electronic, and Control Engineering, IITC, Hankyong National University, 327 Chungang-ro, Anseong-si, Gyeonggi-do 456-749, South Korea

<sup>2</sup>3D Imaging and Display Laboratory, Department of Optics and Optometry & Vision Science, University of Valencia, E46100 Burjassot, Spain

\*Corresponding author: mjcho@hknu.ac.kr

Received 6 August 2018; revised 18 September 2018; accepted 18 September 2018; posted 18 September 2018 (Doc. ID 341465); published 30 October 2018

---

In this paper, we propose a new 3D passive image sensing and visualization technique to improve lateral resolution and depth of field (DoF) of integral imaging simultaneously. There is a resolution trade-off between lateral resolution and DoF in integral imaging. To overcome this issue, a large aperture and a small aperture can be used to record the elemental images to reduce the diffraction effect and extend the DoF, respectively. Therefore, in this paper, we utilize these two pickup concepts with a non-uniform camera array. To show the feasibility of our proposed method, we implement an optical experiment. For comparison in details, we calculate the peak signal-to-noise ratio (PSNR) as the performance metric. © 2018 Optical Society of America

**OCIS codes:** (100.0100) Image processing; (110.6880) Three-dimensional image acquisition; (100.6890) Three-dimensional image processing.

<https://doi.org/10.1364/AO.57.009423>

---

## 1. INTRODUCTION

Integral imaging is one of the passive three-dimensional (3D) imaging techniques for sensing and visualization of real 3D objects [1–7]. Conventional integral imaging consists of pickup and reconstruction. In pickup, 2D images with different perspectives called elemental images can be obtained through a lenslet or camera array. In reconstruction, 3D images can be displayed or reconstructed in 3D space by back-projecting the recorded elemental images through a lenslet or virtual pinhole array. Integral imaging can provide full-color, full-parallax, and continuous viewing points without special glasses and coherent light sources. However, it still has unsolved problems such as low lateral resolution (viewing resolution), narrow viewing angle, and low depth of field (DoF).

To improve these problems, much research has been reported in the past decades [8–32]. Some of these studies have shown better results than conventional integral imaging by adding special devices or by developing image enhancement algorithms [11–17]. However, they can be the source of other problems because they are not cost effective and their implementation may be complicated. In addition, these methods can solve only a single problem of integral imaging. Therefore, it is difficult to improve both lateral resolution and DoF simultaneously.

One of the other studies [18–20] sought to improve 3D resolution by changing the conventional integral imaging method without adding devices and algorithms. The pixels of elemental images rearrangement technique (PERT) [18,19] is a method to improve the visual quality of 3D images by rearranging pixels on the reconstruction plane. In the case of a light field camera [20], a method was suggested to acquire 3D images by locating the microlens array between the imaging lens and the image sensor. This improves resolution by reconstructing the details of the image and refocus the image through digital reconstruction.

These problems in integral imaging are caused by some trade-offs between different system parameters such as the  $f$ -number (ratio between focal length and aperture size) of each lenslet or camera lens, the resolution of the image sensor, the lenslet fill factor, the total parallax of the lenslet or camera array, and so on. For example, when the viewing angle is wide, the DoF is shallow. Also, when the sharpness is improved, the DoF is degraded since there is a trade-off between the spot size and the DoF. Therefore, it is difficult to enhance both lateral resolution and DoF in integral imaging simultaneously.

To partially solve some of these problems in integral imaging, resolution priority integral imaging (RPII) and depth priority integral imaging (DPII) have been reported in Refs. [21–29].

In RPII, the spot size of the 3D image can be minimized (i.e., the best lateral resolution) by setting the distance between the lenslet array and elemental image plane bigger than the focal length of each lenslet. However, the DoF is sacrificed. On the other hand, in DPII, since the distance between the lenslet array and the elemental image plane is the same as the focal length of each lenslet, the DoF can be improved while the lateral spot size becomes the size of each lenslet. It is noticed that the performance of these techniques depends on the system parameters in integral imaging. To optimize these system parameters, integral imaging analysis has been reported in Refs. [21–32]. However, in previous research, there have still been trade-offs between lateral resolution and the DoF. Here, we call these constraints the resolution trade-offs.

In this paper, we propose a new 3D integral imaging technique that can alleviate these resolution constraints in integral imaging. In our proposed method, we try to overcome the resolution trade-off by using non-uniform [30–32] system parameters, such as the  $f$ -number of the lens and sensor size. In addition, we optimize the location of the reference plane by using the hyperfocal distance as the image distance for the lenslets. Note that this distance is the basis for obtaining the practical DoF. In our analysis, the permitted circle of confusion is used as the criteria of resolution trade-off in integral imaging. The effect of diffraction at each lenslet is used to compute the individual blur spot sizes of the 3D images.

This paper is organized as follows. In Section 2, we describe optical image formation and resolution analysis of integral imaging. Then, in Section 3, we present our proposed method with a non-uniform camera array. We show and discuss the experimental results for supporting our proposed method in Section 4. Finally, we conclude with a summary in Section 5.

## 2. LATERAL RESOLUTION AND DOF FOR OPTICAL IMAGE FORMATION

### A. Optical Image Formation

For recording the object scene, a conventional optical imaging system consists of at least a single imaging lens and an image sensor. By adjusting the imaging system parameters, such as the lens parameters (e.g., focal length, aperture size, and shape) and the image sensor parameters (e.g., sensor size, pixel size, and sensitivity), recorded images with various visual qualities can be obtained. In addition, the parameters of the object scene (e.g., size, distance, brightness, sharpness, and so on) are important to determine the imaging system parameters. Lateral resolution is defined as the size of the permitted circle of confusion  $C_p$  [33–36]. This parameter is defined as the largest acceptable spot size diameter that a point is allowed to spread out onto the sensor.

Figure 1 illustrates optical image formation from the geometrical optics point of view. When the imaging lens with focal length  $f$  is ideal, an axial point light source at  $d_o$  from the lens focuses on the image plane at a distance  $d_i$ . According to the Gauss form of the lens equation, these distances are related by the following formula [33]:

$$\frac{1}{d_o} + \frac{1}{d_i} = \frac{1}{f}. \quad (1)$$

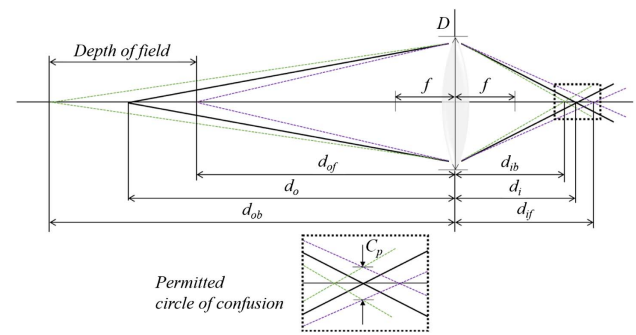


Fig. 1. Optical image formation using geometrical optics for DoF.

When the point light source is located at different distances  $d_{ob}$  and  $d_{of}$  from  $d_o$ , image distances  $d_{ib}$  and  $d_{if}$  are different from the image plane  $d_i$ , respectively. Then, the point light sources at  $d_{ob}$  and  $d_{of}$  form a blur spot in the image plane  $d_i$ . When this spot made by a light coming from an arbitrary distance matches the permitted circle of confusion  $C_p$ , those distances define the limits for the axial (focused) field of the imaging lens. The length of this axial interval is the DoF of the lens. In this case, according to Fig. 1, we can find this spot  $C$  made by a light coming from an arbitrary distance,

$$C = \frac{D|d_i - d_{ib}|}{d_{ib}} = \frac{D|d_{if} - d_i|}{d_{if}}, \quad (2)$$

where  $D$  is the diameter of the lens.

For illustration purposes, let us assume that the permitted circle of confusion is 0.029 mm, which is a conventional value used in the assessment of typical full-frame (36 mm × 24 mm) photographic cameras. Figure 2 shows graphs for the spot size onto the sensor (blue line) at various object distances and for two diameters of the lens aperture (e.g.,  $f/\# = 36, 5.6$ ). We also assume that the fixed focal length is 50 mm and the reference object plane is 250 mm. As the object and focused image distances are different from the reference object and image distances (forward or backward of the object and image planes), respectively, the diameter of the blur spot increases and an image is blurred on the reference image plane. When blur spot matches the permitted circle of confusion, this range is the DoF of the camera. In case of Fig. 2(a), when the diameter of aperture is about 1.4 mm (e.g.,  $f/\# = 36$ ), the DoF is 42.05 mm (dof = 230.73 mm, dob = 272.78 mm). When the diameter of the aperture is about 8.9 mm (e.g.,  $f/\# = 5.6$ ) as shown in Fig. 2(b), the DoF is 6.5 mm (dof = 246.79 mm, dob = 253.29 mm).

From this result, and using Eq. (1), the DoF is given by [33–36]

$$\text{DoF} = |d_{ob} - d_{of}|, \quad (3)$$

$$d_{ob} = \frac{d_o(H - f)}{H + d_o - 2f}, \quad (4)$$

$$d_{of} = \frac{d_o(H - f)}{H - d_o}, \quad (5)$$

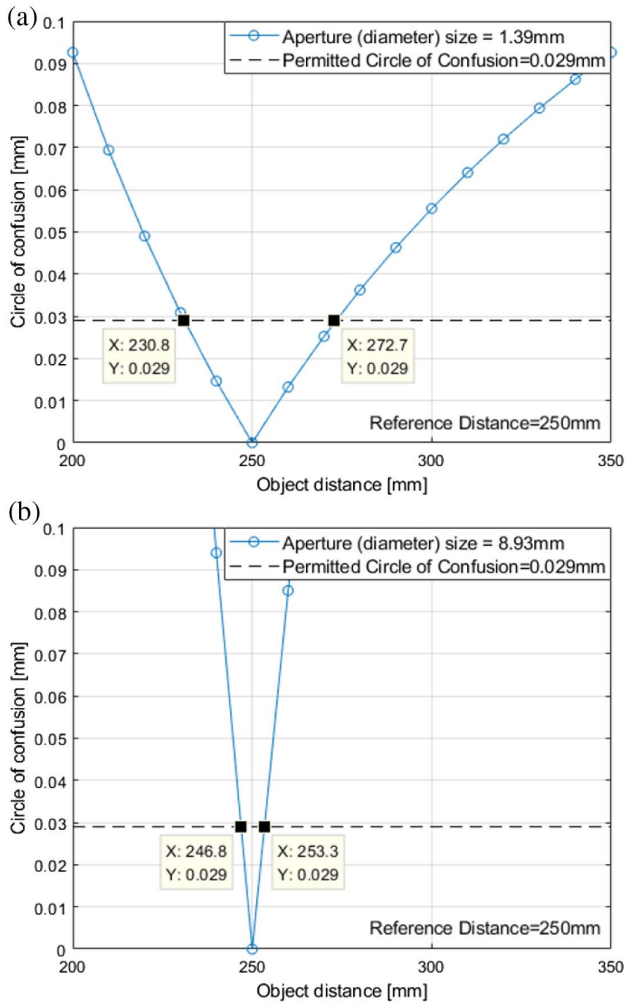


**Fig. 2.** Circle of confusion via various object point light source distances when (a) the diameter of the aperture is about 1.4 mm (e.g.,  $f/\# = 36$ ) and (b) the diameter of the aperture is about 8.9 mm (e.g.,  $f/\# = 5.6$ ).

$$H = \frac{f^2}{(f/\#)C_p} + f, \quad (6)$$

where  $H$  is the so-called hyperfocal distance and  $f/\# = f/D$  is the  $f$ -number of the lens. Note that  $H$  is the focusing distance at which the distance  $d_{of}$  goes to infinity. It is, in fact, the focusing distance that maximizes the effective DoF of the imaging system. It is worth pointing out here that when this *optimized* (respect to the DoF) focusing distance is used, the smaller the value of  $C_p$ , the smaller the DoF. This means that the higher the transverse resolution, the lower the axial range for proper 3D reconstruction, as stated previously. On the other hand, it is straightforward to find from Eqs. (1)–(6) that the higher the aperture  $D$  for a fixed focal length  $f$ , the smaller the DoF.

We investigate the parameters affecting DoF for a more detailed analysis. Figure 3 shows the DoF range according to  $f$ -number, focal length, and diameter of the aperture. As shown in Fig. 3, DoF is large when the  $f$ -number is large.

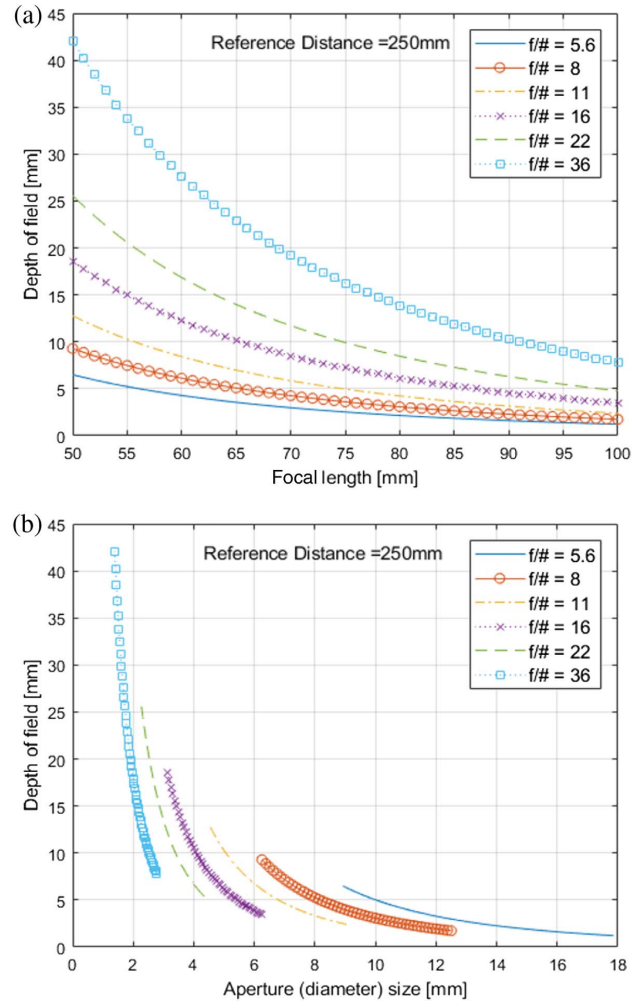


**Fig. 3.** DoF via various parameters. (a) Focal length and (b) diameter of aperture.

It is the same result as shown in Fig. 2. Note that the focal length and the diameter of the aperture are proportional to the  $f$ -number of camera. Figure 3(a) illustrates a relationship between DoF and focal length via various  $f$ -numbers. The longer the focal length, the smaller the DoF because of the fixed  $f$ -number. However, the largest  $f$ -number can obtain the best DoF. As shown in Fig. 3(b), it shows that the smaller diameter of aperture, the larger the DoF in each  $f$ -number. Furthermore, it can be seen that even if the diameter of the aperture size is the same, it has a different DoF value depending on the  $f$ -number. As a result, for a large DoF, we need to set the largest  $f$ -number.

### B. Trade-Off Between Sharpness and DoF of the Integral Imaging System

In the above section, we mentioned the circle of confusion, which is a kind of blur. This is a parameter that defines the DoF range, and it has blurring that affects the image of the object outside the DoF range. We confirm that the circle of confusion value is affected by the diameter of aperture. The Airy disk, which is caused by diffraction, is another kind of blur. This is a parameter that affects the image of the object

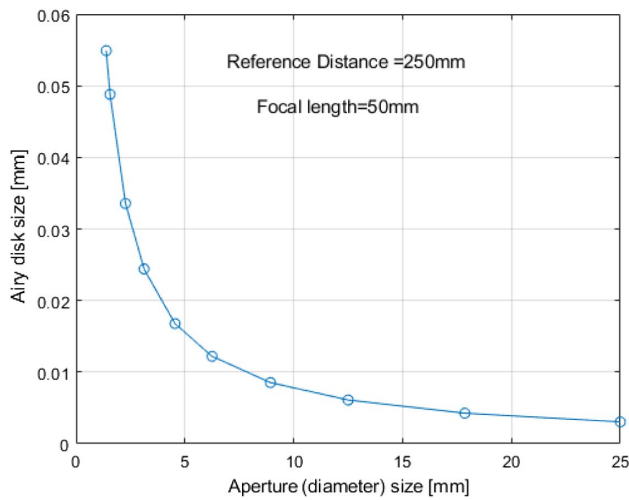


**Fig. 4.** Airy disk via various aperture sizes at the reference image distance  $d_i = 250$  mm.

within the DoF range. This is also affected by the diameter of aperture.

In photography, in fact, the blur value has been considered independent of the aperture size  $D$ . In this paper, however, we will consider the diffraction effect by the finite aperture of the lens. Even though the imaging system is ideal, it creates a minimum blur spot (for perfectly focused images) [36–38]. The Airy disk for a circular clear pupil, as used throughout this paper, is given by

$$A = 2.44 \frac{\lambda \cdot d_i}{D}, \quad (7)$$

where  $\lambda$  is the wavelength of the illumination light. As a result, note that the smaller the blur size, the clearer the image can be maintained.

Figure 4 shows the calculated Airy disk by Eq. (7) via various aperture sizes at the reference image distance  $d_o = 250$  mm. Here, we set  $\lambda = 0.5 \mu\text{m}$ , and the focal length is 50 mm. As the size of the aperture increases (e.g., the value of  $F/\#$  decreases), it shows that the size of Airy disk decreases nonlinearly. We will consider that this minimum blur spot defines the value  $A$  for each aperture diameter of the camera lens within the DoF range. Thus, we can define the resolution trade-off as a function of the aperture size.

Figure 5 shows the Airy disk size depending on focal length and diameter of aperture with a fixed  $f$ -number. As illustrated in Fig. 5, the larger the  $f$ -number, the bigger the Airy disk size. Figure 5(a) represents the Airy disk size via various focal lengths with a fixed  $f$ -number. We can figure out that the shorter the focal length, the smaller the Airy disk size. Figure 5(b) shows the relation between diameter of aperture and the Airy disk size. When the diameter of aperture is getting large, the Airy disk size is also large because focal length changes via fixed  $f$ -number. In addition, if the permitted circle of confusion is 0.029 mm, we should select the  $f$ -number that is smaller than at least  $f/16$  for the sharpness of the image.

As a summary, we have analyzed the relationship of each parameter when the focal length is fixed. For example, in case

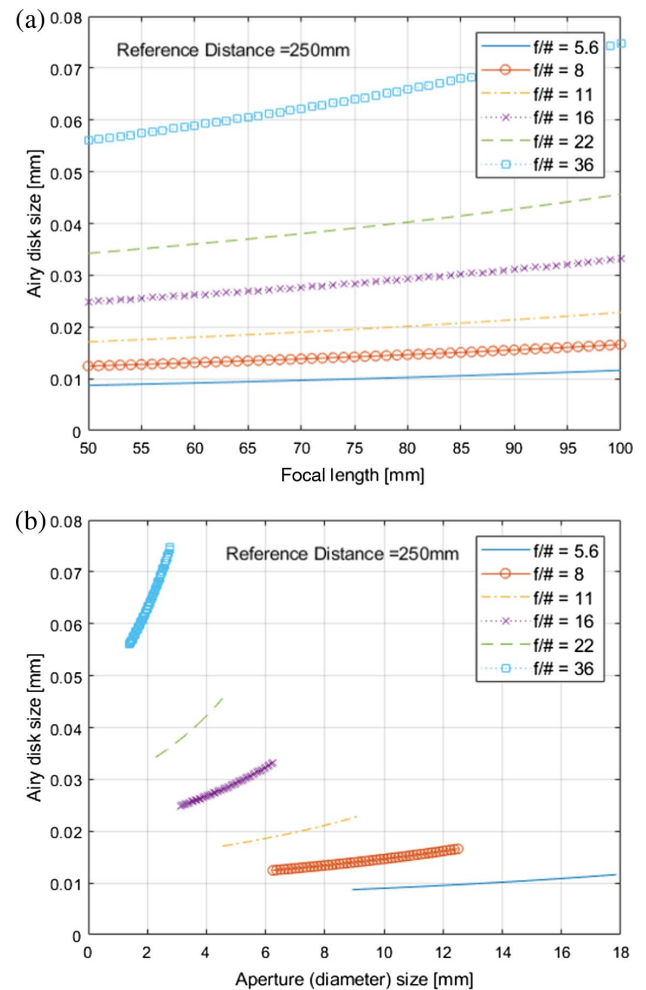


**Fig. 5.** Airy disk size via various parameters. (a) Focal length and (b) diameter of aperture.

of large aperture size, the DoF is shallow, but the spot size of the recorded image on the image sensor is sharp since the permitted circle of confusion range is narrow, as shown in Fig. 2(b), and the diameter of the Airy disk is small, as shown in Fig. 4. On the other hand, when aperture size is small, DoF increases as shown in Fig. 2(a). However, the spot size of the recorded image increases since the diameter of Airy disk is large, as shown in Fig. 4. When the focal length is not fixed within a selected  $f$ -number, we find that there is a precise trade-off relationship. As shown in Fig. 3, the relationship between focal length and DoF is confirmed by using the focal length and diameter of aperture relationship through the  $f$ -number. In addition, not only small diameter size but also large focal length can be known to cause the Airy disk size to increase in Fig. 5. Here, the magnification problem with different focal lengths should also be considered. Therefore, we should select the system parameters through the above analysis. As a result, to combine these resolution trade-off features, in this paper, we propose a new method of integral imaging using a non-uniform camera array where the  $f$ -numbers of the camera lenses are non-uniform.

### 3. THREE-DIMENSIONAL INTEGRAL IMAGING USING NON-UNIFORM CAMERA ARRAY SYSTEM PARAMETERS

The resolution trade-off stated above imposes the limitation that with a single imaging system both lateral resolution and DoF cannot be optimized simultaneously. The two different schemes used in integral imaging (RPII and DPII) can only improve either the lateral resolution or the DoF. Although some optimization of 3D resolution has been addressed by several studies [8–10,30–32], this resolution trade-off has not yet been overcome.

The proposed method for improving the resolution trade-off is divided by two steps based on computational integral imaging. First, the pickup step of the proposed method generates elemental images with various parameter values. Then, in the proposed reconstruction step, reconstructed images are produced by combining with all elemental images.

#### A. Elemental Image Pickup Using Non-Uniform System Parameters

For obtaining the elemental images, we consider here a camera array system instead of a lenslet array system since it is easier to adjust the system parameters such as the focal length, aperture size, and focusing distance. The elemental images are the most important information for the 3D performance of integral imaging since they include the lateral resolution and DoF of the 3D images. To obtain more accurate reconstructed 3D images, computational volumetric reconstruction [8] is utilized. Thus, in this paper, we design our proposed method based on the conventional 3D image method [i.e., synthetic aperture integral imaging (SAII) [9] and computational volumetric reconstruction].

Figure 6 illustrates the pickup process of our proposed method with a non-uniform camera array. To improve the DoF for 3D images, a camera array with large  $f$ -number (i.e., small aperture size for a fixed focal length) is used in SAII as shown in Fig. 6(a). Thus, elemental images with a large DoF can be obtained. Then, cameras with a small  $f$ -number are placed between the camera arrays as shown in Fig. 6(b), which appear as non-uniform camera arrays. These cameras record the elemental images by changing the focusing distance according to the distance of the objects.

Our proposed system, as depicted in Fig. 6, can expand the reconstruction range with sufficient lateral resolution for 3D reconstructed images since it can reduce the diffraction of the small aperture and enhance the visual quality of each 3D object by the small Airy disk size of the large aperture. Thus, elemental images for the enhancement of both lateral resolution and DoF are obtained via the pickup process of our proposed method.

We need to consider the gap between cameras for the total parallax when 3D objects are located very close to the camera array (e.g., closer than the focal length of camera array). In general, 3D objects are located after the focal length. However, if 3D objects are very close to camera array, elemental images have only a part of the 3D objects; it depends on the position and size of the 3D objects. For example, when the size of the 3D objects is 100 mm  $\times$  100 mm and the position of 3D object is closer than the focal length of camera array, the gap between

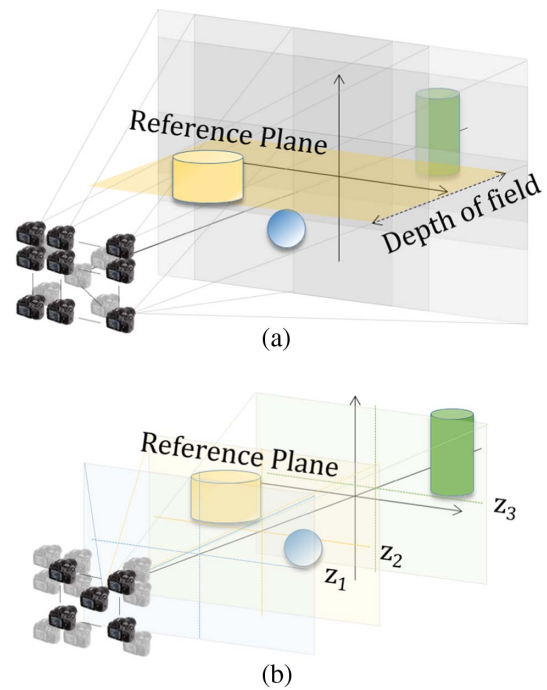


**Fig. 6.** Pickup process of our proposed method for both (a) DoF and (b) lateral resolution of 3D objects.

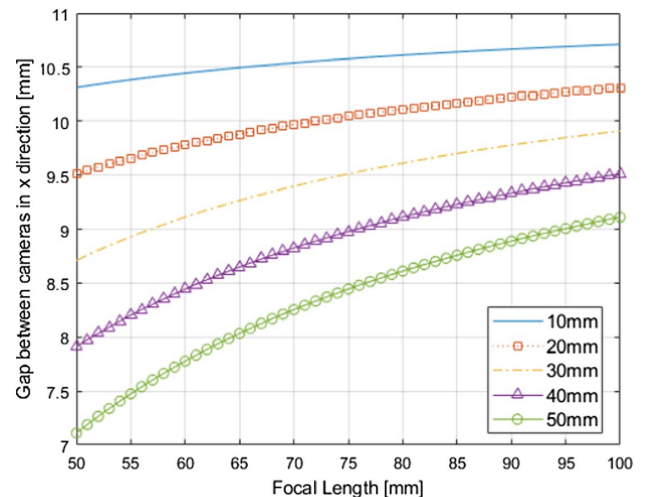


**Fig. 7.** Gap between cameras when 3D objects are located at a closer distance than the focal length of the camera array.

cameras for different positions of 3D objects should be adjusted as shown in Fig. 7.

In Fig. 7, as the focal length increases, a larger gap is required because of the narrow field of view. In addition, as the object distance increases, the gap between cameras decreases because object size in the image decreases.

#### B. Reconstruction of 3D Images with Non-Uniform System Parameters

To generate the reconstructed 3D images using these elemental images, in this paper, we use computational volumetric reconstruction.

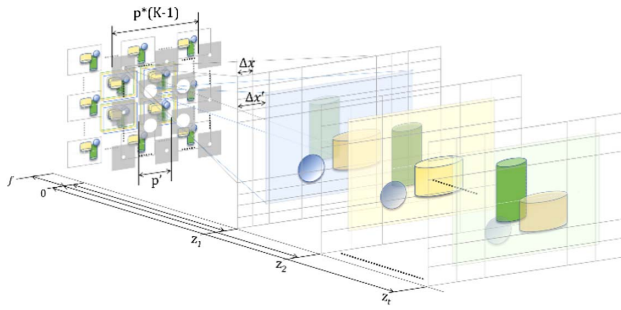


**Fig. 8.** Reconstruction process of our proposed method.

Figure 8 illustrates the method based on the computational volumetric reconstruction in our proposed method. First, the reconstructed 3D images with the large DoF,  $R^{(D)}(x, y, z)$ , are generated using conventional computational reconstruction with elemental images obtained by a large  $f$ -number SAIL,  $EI_{kl}^{(D)}$ , as shown in Fig. 6(a),

$$R^{(D)}(x, y, z) = \frac{1}{O(x, y, z)} \left[ \sum_{k=0}^{K-1} \sum_{l=0}^{L-1} EI_{kl}^{(D)}(x + k\Delta x, y + l\Delta y) \right], \quad (8)$$

$$\Delta x = \frac{N_x f p}{c_x z}, \quad \Delta y = \frac{N_y f p}{c_y z}. \quad (9)$$

Then, the final reconstructed 3D image at reconstruction depth  $z_t$  in our proposed method,  $R(x, y, z_t)$ , is generated by adding the elemental image obtained by a small  $f$ -number SAIL,  $EI_{k'l'}(R, z_t)$ , to the reconstructed 3D image at reconstruction depth  $z_t$ ,  $R^{(D)}(x, y, z)$ . The following equations describe a 3D image reconstruction of our proposed method:

$$R(x, y, z_t) = \frac{1}{O_t(x, y, z_t)} \sum_{k'=0}^{K'-1} \sum_{l'=0}^{L'-1} [R^{(D)}(x, y, z_t) + EI_{k'l'}^{(R, z_t)}(x' + k'\Delta x', y' + l'\Delta y')], \quad (10)$$

$$\Delta x' = \frac{N_x f p'}{c_x z_t}, \quad \Delta y' = \frac{N_y f p'}{c_y z_t}, \quad (11)$$

where  $R(x, y, z_t)$  is the final reconstructed 3D image of our proposed method,  $(k, l)$  and  $(k', l')$  are the indexes of elemental images obtained from Figs. 6(a) to 6(b),  $R^{(D)}(x, y, z)$  are the reconstructed 3D images by large  $f$ -number,  $O(x, y, z)$  and  $O_t(x, y, z_t)$  are the overlapping matrices at the reconstruction depth  $z_t$ ,  $(\Delta x, \Delta y)$  and  $(\Delta x', \Delta y')$  are the shifting pixels for reconstruction in Figs. 6(a) and 6(b),  $N_x, N_y$  are the number of pixels for each elemental image,  $f$  is the focal length of the camera,  $p, p'$  are the gaps between cameras in Figs. 6(a) and 6(b), and  $c_x, c_y$  are the image sensor dimensions of the camera, respectively.

#### 4. EXPERIMENTAL RESULTS AND DISCUSSION

To show the feasibility of our proposed method, we implement some optical experiments. Figure 9(a) shows the experimental setup where three different objects are located at  $z_1 = 305$  mm,  $z_2 = 420$  mm, and  $z_3 = 540$  mm from the

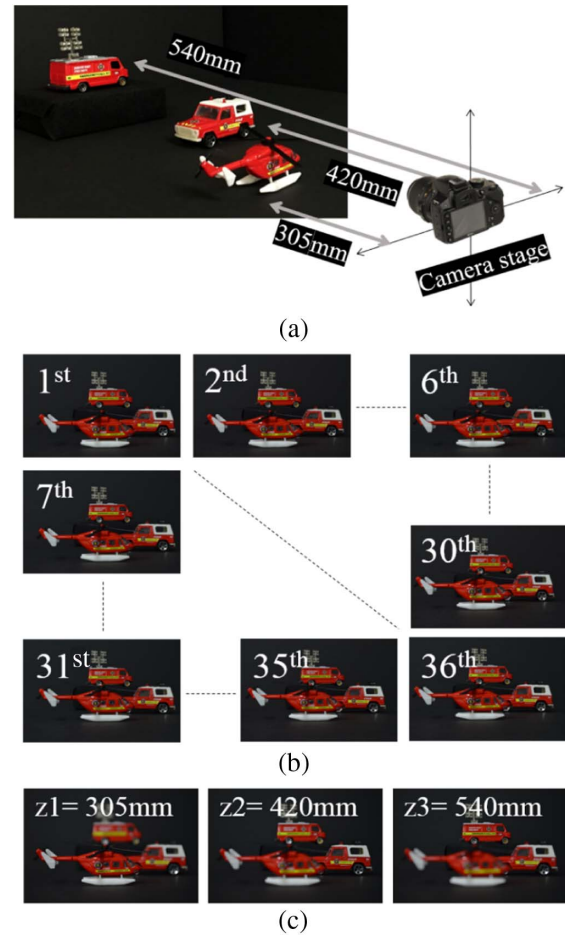


**Fig. 9.** (a) Experimental setup, (b) elemental images with  $f/36$ , and (c) elemental images with  $f/5.6$ .

camera (Nikon D3200). The  $f$ -numbers of the lens in our proposed method are set to  $f/36$  and  $f/5.6$ . The total parallax of our proposed pickup system with  $f/36$  is  $12 \text{ mm} \times 12 \text{ mm}$ , and each camera position gap is 2 mm. In the case of the camera with  $f/5.6$ , we use one camera for convenience (i.e.,  $k'$  and  $l'$  are zero), so it is at the center of the array in our proposed pickup. It does not overlap with the camera array of  $f/36$ . Figures 9(b) and 9(c) show the elemental images obtained with our proposed pickup process with two different  $f$ -numbers. In this experiment, the elemental images have a  $f/5.6$  focus on each object. By using  $f/36$  we capture a set of  $6 \times 6$  elemental images. Each elemental image is  $3008 \times 2000$  pixels. Note that when we obtain elemental images, we need to control the exposure time of the camera to obtain the same brightness for elemental images with different  $f$ -numbers.

Figure 10 shows the elemental images focused on 420 mm with different  $f$ -number settings. It is noticed that elemental images captured with  $f/36$  have a larger DoF from the first object to the third object and worse lateral resolution than the elemental image registered using  $f/5.6$ .

Table 1 shows the DoF with various  $f$ -numbers and focusing distances for this value of permitted circle of confusion  $C_p$ . Our image sensor, Nikon D3200, has an APS-C type sensor, whose size is  $23.2 \text{ mm} \times 15.4 \text{ mm}$ . The diameter of the



**Fig. 10.** Comparison between elemental images by  $f/36$  (left) and  $f/5.6$  (right) at a distance of 420 mm.

permitted circle of confusion is 0.0187 mm in this case. In the SAIL system with  $f/36$ , the camera array focuses on the object at 420 mm. Thus, sharp elemental images can be recorded from 381.95 to 466.48 mm. On the other hand, in the SAIL system with  $f/5.6$ , the camera focuses on each object to record an elemental image with a small DoF, as shown in Table 1.

Figure 11 shows the reconstructed 3D images of the three different methods: the conventional method with elemental images by  $f/36$ , the conventional method with elemental images by  $f/5.6$ , and our proposed method. As shown in Figs. 11(a) and 11(b), the reconstructed 3D images by the conventional method with a  $f/36$  SAIL have larger depth range than the reconstructed 3D images by the conventional method with a  $f/5.6$  SAIL. On the other hand, at a distance of 420 mm, the reconstructed 3D image in Fig. 11(a) has lower lateral resolution than the reconstructed 3D images in Fig. 11(b) due to diffraction in the lens aperture. Figure 11(c) shows the reconstructed 3D images by our proposed method. They have both sufficient lateral resolution and DoF compared with the others. Therefore, it is proved that our method can enhance the resolution trade-off in integral imaging.

To show the 3D resolution improvement obtained with our technique objectively, we calculate the peak signal-to-noise ratio (PSNR) as the performance metric, defined as [39]

$$\text{PSNR} = 20 \cdot \log_{10} \left( \frac{I_{\max}}{\sqrt{\text{MSE}}} \right), \quad (12)$$

$$\text{MSE} = \frac{1}{n} \sum (I_{\text{out}} - I_{\text{ref}})^2, \quad (13)$$

where  $I_{\max}$  is the maximum possible pixel value of the image,  $I_{\text{out}}$  is the resulting image of proposed method,  $I_{\text{ref}}$  is the

**Table 1.** Depth of Field

	$F/36$	$F/5.6$
$z = 305$ mm	—	6.51 mm (301.78–308.29 mm)
$z = 420$ mm	84.53 mm (381.95–466.48 mm)	13.02 mm (413.59–426.61 mm)
$z = 540$ mm	—	22.18 mm (529.13–551.31 mm)

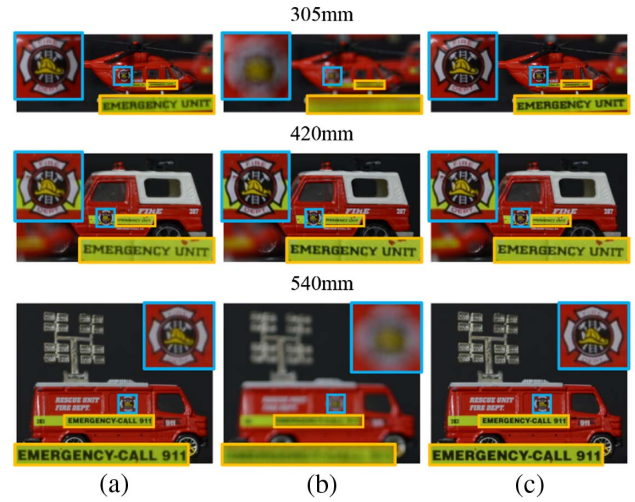


**Fig. 11.** Reconstructed 3D images by (a) conventional method with elemental images by  $f/36$ , (b) conventional method with elemental images by  $f/5.6$ , and (c) our proposed method.

**Table 2.** PSNR of the Reconstructed Images at Object Positions

PSNR [dB]	Conventional Method	Proposed Method
$z = 305$ mm	23.6725	29.2539
$z = 420$ mm	28.9614	33.2696
$z = 540$ mm	27.1402	32.0652

reference image, and  $n$  is the number of pixels for the image.

Table 2 represents PSNR values for both the conventional method and our proposed method at different object positions. It is noticed that our proposed method has better performance than the conventional method with an approximately 2–5 dB difference.

Figure 12 depicts the graph of PSNR via various reconstruction depths: the conventional method (with only

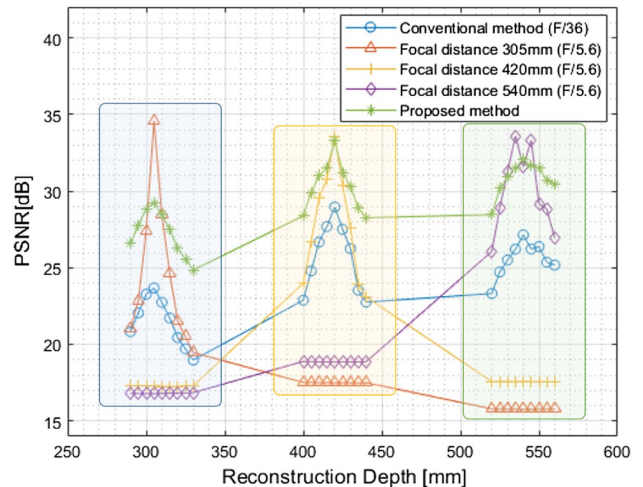


**Fig. 12.** Peak signal-to-noise ratio (PSNR) via various reconstruction depths.

$f/36$ ), three conventional methods using elemental images focused on each object (with only  $f/5.6$ ), and our proposed method. As shown in Fig. 12, each rectangular area is a section in which an elemental image by  $f/5.6$  of each object is used:  $z = 305$  mm is blue,  $z = 420$  mm is orange, and  $z = 540$  mm is green. It shows that the PSNR values of the reconstructed images with  $f/5.6$  are larger than the reconstructed image of  $f/36$ . This means that the lateral resolutions of the reconstructed 3D images with  $f/5.6$  are better than those with  $f/36$  on each object distance. In addition, the PSNRs of our proposed method are approximately 2–5 dB bigger than the PSNR of the conventional results with  $f/36$ . As a result, we confirm that our proposed method can enhance the resolution trade-off throughout all reconstruction depths.

## 5. CONCLUSIONS

In this paper, we have proposed a new 3D passive image sensing and visualization method with enhanced lateral resolution and DoF in integral imaging simultaneously. We have analyzed the resolution trade-off in integral imaging by using a combination of geometrical optics and wave optics. By using non-uniform system parameters, we have alleviated the resolution trade-off in integral imaging. To support our claim, we have implemented some optical experiments with various SAIIs. This method can easily improve both lateral resolution and DoF (i.e., the resolution trade-off). In addition, we can find the appropriate system parameters of the 3D imaging system by considering the analysis results for a non-uniform system of integral imaging. The proposed method may be utilized for various applications from macroscopic to microscopic systems. However, there are some issues that should be solved in future work. In our experiment, although the camera system presented a wider depth tolerance than the calculated DoF, the depth improvement in the experimental result was not dramatic. We also need a clear definition of the relationship between image resolution and the parameters. In order to improve other issues, we will study these methods in the future.

**Funding.** National Research Foundation of Korea (NRF) (2017K1A3A1A19070753, 2017R1D1A1B03030343); Ministerio de Economía, Industria y Competitividad, Gobierno de España (DPI2015-66458-C2-1-R); Generalitat Valenciana (PROMETEOII/2014/072).

## REFERENCES

- B. Javidi, F. Okano, and J.-S. Son, *Three-Dimensional Imaging, Visualization, and Display* (Springer, 2009).
- T. Okoshi, *Three-Dimensional Imaging Techniques* (Academic, 1976).
- A. Stern and B. Javidi, "Three-dimensional image sensing, visualization, and processing using integral imaging," *Proc. IEEE* **94**, 591–607 (2006).
- G. Lippmann, "La photographie integrale," *C. R. Acad. Sci.* **146**, 446–451 (1908).
- F. Okano, H. Hoshino, J. Arai, and I. Yuyama, "Real-time pickup method for a three-dimensional image based on integral photography," *Appl. Opt.* **36**, 1598–1603 (1997).
- H. Arimoto and B. Javidi, "Integral three-dimensional imaging with digital reconstruction," *Opt. Lett.* **26**, 157–159 (2001).
- M. Cho, M. Daneshpanah, I. Moon, and B. Javidi, "Three-dimensional optical sensing and visualization using integral imaging," *Proc. IEEE* **99**, 556–575 (2011).
- J. S. Jang and B. Javidi, "Three-dimensional synthetic aperture integral imaging," *Opt. Lett.* **27**, 1144–1146 (2002).
- S. H. Hong, J. S. Jang, and B. Javidi, "Three-dimensional volumetric object reconstruction using computational integral imaging," *Opt. Express* **12**, 483–491 (2004).
- F. Okano, J. Arai, K. Mitani, and M. Okui, "Real-time integral imaging based on extremely high resolution video system," *Proc. IEEE* **94**, 490–501 (2006).
- Y. Piao, M. Zhang, X. Wang, and P. Li, "Extended depth of field integral imaging using multi-focus fusion," *Opt. Commun.* **411**, 8–14 (2018).
- M. Zhang, C. Wei, Y. Piao, and J. Liu, "Depth-of-field extension in integral imaging using multi-focus elemental images," *Appl. Opt.* **56**, 6059–6064 (2017).
- H. Navarro, G. Saavedra, M. Martinez-Corral, M. Sjoström, and R. Olsson, "Depth-of-field enhancement in integral imaging by selective depth-deconvolution," *J. Disp. Technol.* **10**, 182–188 (2014).
- Y. J. Wang, X. Shen, Y. H. Lin, and B. Javidi, "Extended depth-of-field 3D endoscopy with synthetic aperture integral imaging using an electrically tunable focal-length liquid-crystal lens," *Opt. Lett.* **40**, 3564–3567 (2015).
- K. C. Kwon, M. U. Erdenebat, M. A. Alam, Y. T. Lim, K. G. Kim, and N. Kim, "Integral imaging microscopy with enhanced depth-of-field using a spatial multiplexing," *Opt. Express* **24**, 2072–2083 (2016).
- Z. Wang, A. Wang, S. Wang, X. Ma, and H. Ming, "Resolution-enhanced integral imaging using two micro-lens arrays with different focal lengths for capturing and display," *Opt. Express* **23**, 28970–28977 (2015).
- B. Cho, P. Kopycki, M. Martinez-Corral, and M. Cho, "Computational volumetric reconstruction of integral imaging with improved depth resolution considering continuously non-uniform shifting pixels," *Opt. Laser Eng.* **111**, 114–121 (2018).
- M. Cho and B. Javidi, "Computational reconstruction of three-dimensional integral imaging by rearrangement of elemental image pixels," *J. Disp. Technol.* **5**, 61–65 (2009).
- K. Inoue, M. C. Lee, B. Javidi, and M. Cho, "Improved 3D integral imaging reconstruction with elemental image pixel rearrangement," *J. Opt.* **20**, 025703 (2018).
- T. E. Bishop and P. Favaro, "The light field camera: extended depth of field, aliasing, and superresolution," *IEEE Trans. Pattern Anal. Mach. Intell.* **34**, 972–986 (2012).
- J. S. Jang and F. Jin, "Three-dimensional integral imaging with large depth of field by use of real and virtual image fields," *Opt. Lett.* **28**, 1421–1423 (2003).
- H. Hoshino, F. Okano, H. Isono, and I. Yuyama, "Analysis of resolution limitation of integral photography," *J. Opt. Soc. Am. A* **15**, 2059–2065 (1998).
- J. S. Jang and B. Javidi, "Improved viewing resolution of three-dimensional integral imaging by use of nonstationary micro-optics," *Opt. Lett.* **27**, 324–326 (2002).
- C. G. Luo, X. Xiao, M. Martinez-Corral, C. W. Chen, B. Javidi, and Q. H. Wang, "Analysis of the depth of field of integral imaging displays based on wave optics," *Opt. Express* **21**, 31263–31273 (2013).
- F. Jin and J.-S. Jang, "Effects of device resolution on three-dimensional integral imaging," *Opt. Lett.* **29**, 1345–1347 (2004).
- D. H. Shin, S. H. Lee, and E. S. Kim, "Optical display of true 3D objects in depth-priority integral imaging using an active sensor," *Opt. Commun.* **275**, 330–334 (2007).
- M. Martinez-Corral and B. Javidi, "Fundamentals of 3D imaging and displays: a tutorial on integral imaging, lightfield, and plenoptic systems," *Adv. Opt. Photon.* **10**, 512–566 (2018).
- M. Martínez-Corral, A. Dorado, J. C. Barreiro, G. Saavedra, and B. Javidi, "Recent advances in the capture and display of macroscopic and microscopic 3-D scenes by integral imaging," *Proc. IEEE* **105**, 825–836 (2017).
- X. Shen, A. S. Markman, P. Latorre-Carmona, A. Martínez-Uso, J. M. Sotoca, F. Pla, M. Martínez-Corral, G. Saavedra, Y. P. Huang, A. Stern, and B. Javidi, "Multidimensional optical sensing and imaging

- systems (MOSIS): from macro to micro scales," *Proc. IEEE* **105**, 850–875 (2017).
30. J. S. Jang and B. Javidi, "Large depth-of-focus time-multiplexed three-dimensional integral imaging by use of lenslets with nonuniform focal lengths and aperture sizes," *Opt. Lett.* **28**, 1924–1926 (2003).
  31. S. C. Kim, C. K. Kim, and E.-S. Kim, "Depth-of-focus and resolution-enhanced three-dimensional integral imaging with non-uniform lenslets and intermediate-view reconstruction technique," *3D Research* **2**, 1–9 (2011).
  32. H. Navarro, J. C. Barreiro, G. Saavedra, M. Martínez-Corral, and B. Javidi, "High-resolution far-field integral-imaging camera by double snapshot," *Opt. Express* **20**, 890–895 (2012).
  33. E. Hecht, *Optics*, 5th ed. (Pearson, 2016).
  34. R. E. Jacobson, S. Ray, G. G. Attridge, and N. Axford, *The Manual of Photography: Photographic and Digital Imaging*, 9th ed. (2000).
  35. H. M. Merklinger, *The INs and OUTs of Focus*, Internet ed. (2002).
  36. V. Aslantas and D. T. Pham, "Depth from automatic defocusing," *Opt. Express* **15**, 1011–1023 (2007).
  37. J. W. Goodman, *Introduction to Fourier Optics*, 2nd ed. (McGraw-Hill, 1996).
  38. J. E. Greivenkamp, "Airy disk," in *Field Guide to Geometrical Optics* (SPIE, 2004).
  39. Q. Huynh-Thu and M. Ghanbari, "Scope of validity of PSNR in image/video quality assessment," *Electron. Lett.* **44**, 800–801 (2008).